Article

Photocatalytic Recovery of Gold from a Non-Cyanide Gold Plating Solution as Au Nanoparticle-Decorated Semiconductors

Naphaphan Kunthakudee, Tarawipa Puangpetch, Prakorn Ramakul, and Mali Hunsom*

Read Online

ACCESS | Metrics & More | Article Recommendations

ABSTRACT: In this work, a photocatalytic process was carried out to recover gold (Au) from the simulated non-cyanide plating bath solution. Effects of semiconductor types (TiO_2, WO_3, Nb_2O_3, CeO_2, and Bi_2O_3), initial pH of the solution (3–10), and type of complexing agents ($Na_2S_2O_3$ and Na_2SO_3) and their concentrations (1–4 mM each) on Au recovery were explored. Among all employed semiconductors, TiO_2 exhibited the highest photocatalytic activity to recover Au from the simulated spent plating bath solution both in the absence and presence of complexing agents, in which Au was completely recovered within 15 min at a pH of 6.5. The presence of complexing agents remarkably affected the size of deposited Au on the TiO_2 surface, the localized surface plasmon effect (LSPR) behavior, and the valence band (VB) edge position of the obtained Au/TiO_2, without a significant change in the textural properties or the band gap energy. The photocatalytic activity of the obtained Au/TiO_2 tested via two photocatalytic processes depended on the common reduction mechanism rather than the textural or optical properties. As a result, the Au/TiO_2 NPs obtained from the proposed recovery process are recommended for use as a photocatalyst for the reactions occurring at the conduction band rather than at the valence band. Notably, they exhibited good stability after the fifth photocatalytic cycle for Au recovery from the actual cyanide plating bath solution.
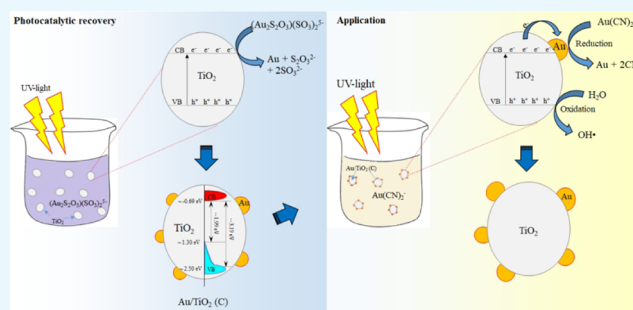
1. INTRODUCTION

Gold (Au) plating is an essential process used to prepare the surface of some electronic parts in the printed circuit boards (PCBs) owing to its high electrical conductivity, high reliability, excellent planarity, good solderability, and high corrosion resistance.[1,2] A high growth rate of the electronics industry is predicted to be observed in our country during 2021–2023 due to a number of various technological developments, such as the rollout of the 5G technology, the increase of smart car markets, and consumer demand for portable computers (PCs), notebooks, tablets, and smartphones, resulting from work from home (WFH) and distance learning of students during the COVID-19 situation.[3] Typically, Au plating can be carried out via both cyanide and non-cyanide Au salts by electroplating or electroless plating. The electrolytic Au cyanide plating can be operated in a wide pH range from acidic to alkaline pH, while non-cyanide plating is effective at neutral or alkaline pH.[1] To achieve a stable plating system, various kinds of complexing agents and additives are employed to obtain a good quality of plated specimens.[1,4] Thus, the spent plating bath solution generated from the process contains various kinds of chemicals and metal ions such as chromium (Cr), copper (Cu), iron (Fe), or nickel (Ni) ions, as well as the residual Au complex. The presence of precious metals such as Au in the effluent is an economic loss.

Thus, various processes have been developed to recover Au from the discharged solution, such as precipitation, electrolysis, adsorptive reduction, ion exchange, solvent extraction, and bioproduction and biorecovery.[5,6] In addition to the mentioned processes, another promising process that can be used to recover Au from the plating bath solution is the photocatalytic process because it possesses the viability to recover Au from aqueous solutions of both chloride species[7] and cyanide species.[8] In addition, it is environmentally friendly, involves low operating costs, and can operate at ambient conditions.[9,10]

The photocatalytic process is a chemical process that occurs under the joint action between light and a photocatalyst.[11,12] The transition-metal oxides or semiconductors such as TiO_2, ZnO, WO_3, etc., are generally used as a photocatalyst because they have no energy levels to promote the recombination of the photogenerated electron (e^-) and hole (h^+) in their

structure. The process efficiency depends upon various parameters, including the redox potential of dissolved metals relative to the utilized semiconductor, the presence of electron and/or hole scavengers, irradiated light intensity, solution pH, and type and loading of utilized semiconductors.[13] Recently, it was reported that TiO_2/SiO_2 exhibited a higher photocatalytic removal of Au(I) from gold−cyanide complexes than bare TiO_2. The presence of hole scavengers such as methanol can promote the deposition of metallic Au on the surface of the utilized photocatalyst.[8] Using an amphiphilic photocatalyst based on a polyoxometallate $(W_{10}O_{32}{}^{4-})$/surfactant (dimethyldioctadecyl ammonium) hybrid, the photocatalytic recovery of Au can be carried out under the pH value of 3−6 and depended on the catalyst loading and concentration of sacrificial agents.[14] The photoreduction of Au(III) via TiO_2 increased with the increase of reaction times and photocatalyst loadings.[15] However, excessive loading of TiO_2 increased the solution turbidity, which decreased the exposure of TiO_2 with the light irradiation. The photoreduction decreased with the increase of the initial concentration of Au(III). The presence of Ag(I) and Cu(II) decreased the photoreduction of Au(III) due to the competition in adsorption and reduction, while the presence of Fe(III) can enhance the photoreduction due to the reduction and quick oxidation of Fe(II). The tannin (TA)-TiO_2 heterostructure induced a high selectivity of Au(III) adsorption, which can prolong the lifetimes of excited electrons and then allow the adsorption/reduction of Au(III) from the solution.[16]

As mentioned above, Au plating can be carried out via both cyanide and non-cyanide baths. The traditional cyanide bath has been successful for a long time in comparison with the non-cyanide bath because it exhibits more outstanding strengths, including high bath stability and superior performance of obtaining gold films with excellent properties.[1,17] However, the development of cyanide baths is currently restricted due to their toxicity and material compatibility problems.[1,18] Thus, a safe and environmentally friendly process or a non-cyanide bath is currently gaining attention. With the increase of the industrial demand for electroless plating via non-cyanide baths, a large quantity of wastewater is produced. Based on our knowledge, very limited work related to Au recovery from a non-cyanide bath effluent by the photocatalytic process is published. For example, Chen et al.[19] attempted to recover Au(I) from a thiosulfate solution using the defect-rich MoS_2 (DR-MoS_2) nanoflowers. It was found that the efficiency of the utilized photocatalyst for the Au(I) reduction can be improved with the aid of ultrasonic treatment. The selective deposition of Au nanoparticles (NPs) on the surface of MoS_2 was promoted by the edge sites and S defects of DR-MoS_2 nanoflowers.

In this work, to aid the generation of Au-containing effluent from non-cyanide plating baths, the photocatalytic recovery of Au from the simulated spent plating bath solution was explored via various semiconductors. The effect of initial solution pH, irradiation time, and types and concentrations of complexing agents was explored. Finally, the photocatalytic activity of the obtained Au NP-decorated semiconductor that exhibited the best photocatalytic recovery of Au from the non-cyanide plating bath was tested via two photocatalytic processes, including the methylene blue (MB) degradation and the Au recovery from actual spent cyanide plating bath solution.

2. RESULTS AND DISCUSSION

2.1. Morphology of Utilized Commercial Semiconductors. The crystal structure of all utilized semiconductors was first evaluated by XRD analysis. As demonstrated in Figure 1a, the XRD pattern of the parent TiO_2 displayed diffraction
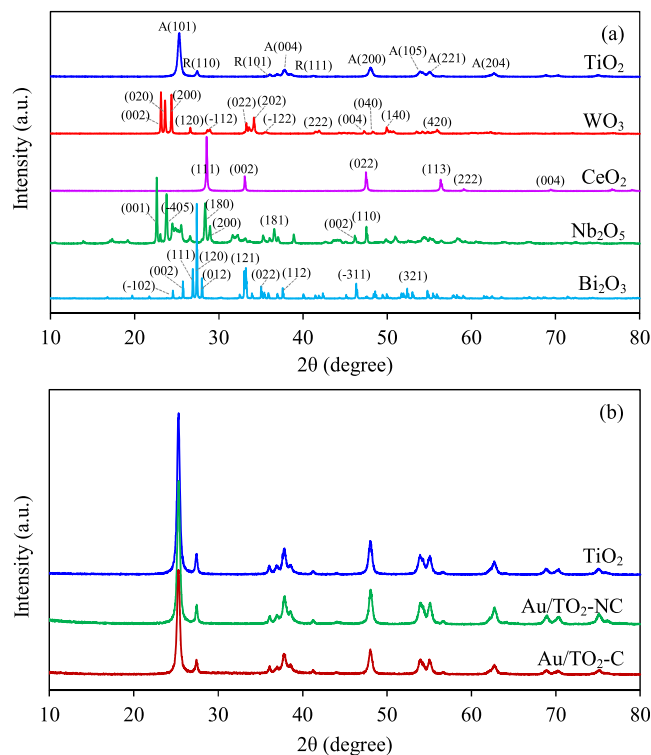
Figure 1. Representative XRD patterns of (a) commercial semiconductors and (b) Au/TiO_2 obtained from the photocatalytic recovery of Au from the simulated spent plating bath solution in the absence and presence of complexing agents at a semiconductor loading of 4 g/L and a light intensity of 4.1 mW/cm².

peaks at 2θ values of 25.3, 37.8, 48.0, 53.90, 55.10, and 62.70°, corresponding to the crystal planes of (101), (004), (200), (105), (221), and (204), respectively, (JCPDS file no. 21-1272) for the anatase phase and displayed 2θ values of 27.41, 36.06, and 41.21°, corresponding to the crystal planes of (110), (101), and (111), respectively, (JCPDS file no. 21-1276) for the rutile phase. For WO_3, its XRD pattern showed the diffraction peaks of the monoclinic phase at 2θ values of 23.07, 23.56, 24.31, 26.54, 28.87, 33.21, 34.12, 35.37, 41.84, 47.21, 48.32, 49.88, and 55.90°, corresponding to the crystal planes of (002), (020), (200), (120), ($\bar{1}$12), (022), (202), ($\bar{1}$22), (222), (004), (040), (140), and (420), respectively, (JCPDS file no. 43-1035). The CeO_2 revealed XRD peaks at 2θ values of 28.54, 33.07, 47.47, 56.31, and 59.08°, corresponding to the crystal planes of (111), (200), (220), (311), and (222), respectively, (JCPDS file no. 340394). For Nb_2O_5, its XRD pattern exhibited the diffraction peak of both orthorhombic and monoclinic phases. The characteristic peaks of the orthorhombic phase appeared at 2θ values of 22.55, 28.30, 28.91, 36.49, 46.09, and 47.47°, corresponding to the crystal planes of (001), (180), (200), (181), (002), and (110), respectively, (JCPDS file no. 71-0336) and the monoclinic structure exhibited a peak at a 2θ of 23.72°, indicating the crystal plane of ($\bar{4}$05) (JCPDS file no. 37-1468). The XRD pattern of Bi_2O_3 showed the main characteristic peaks of the α-

Table 1. Properties of the Commercial Semiconductors and Obtained Au/TiO$_2$

| photocatalysts | crystallite size of the semiconductor[a] (nm) | anatase content (%) | textural property | | | band gap energy (eV) | decorated Au[b] (wt %) | particle size of Au[c] (nm) |
			BET area (m^2/g)	average pore size (nm)	total pore volume (cm^3/g)			
TiO$_2$	21.26	85.84	52.38	5.43	0.0629	3.35		
WO$_3$	77.01		0.595	4.60	0.0005	2.65		
CeO$_2$	54.66		5.432	5.46	0.0065	3.00		
Nb$_2$O$_5$	62.33		2.487	4.96	0.0021	3.14		
Bi$_2$O$_3$	116.82		0.141	1.93	0.0004	2.75		
Au/TiO$_2$-NC	22.94	84.89	55.42	6.83	0.0875	3.20	1.37 ± 0.02	10.3 ± 3.07
Au/TiO$_2$-C	21.43	84.28	56.05	7.02	0.0896	3.19	1.02 ± 0.03	4.23 ± 1.84

[a]Estimated from XRD analysis using Scherrer's equation at crystal planes of (101), (002), (111), (001), and (111) for TiO$_2$, WO$_3$, CeO$_2$, Nb$_2$O$_5$, and Bi$_2$O$_3$, respectively. [b]Estimated from SEM-EDX analysis. [c]Estimated from HRTEM analysis.

monoclinic phase at 2θ values of 24.51, 25.71, 26.88, 27.35, 27.96, 33.21, 35.01, 37.58, 46.28, and 52.35°, corresponding to the crystal planes of ($\bar{1}$02), (002), (111), (120), (012), (121), (022), (112), ($\bar{3}$11), and (321), respectively, (JCPDS file no. 71-2274). The crystallite sizes of all employed semiconductors estimated using Scherrer's equation are listed in Table 1 and can be ranked in the order Bi$_2$O$_3$ > WO$_3$ > Nb$_2$O$_5$ > CeO$_2$ > TiO$_2$.

In the heterogeneous photocatalytic process, the adsorption of active species on the surface of semiconductors must occur first, followed by the photocatalytic reaction. The presence of a high specific surface area can induce effective charge adsorption as well as the photocatalytic activity of the utilized photocatalysts.[20] The N$_2$ adsorption/desorption isotherms of all employed commercial semiconductors are shown in Figure 2a. All explored semiconductors exhibited the type IV isotherm according to the IUPAC classification with H4-shaped

hysteresis loops, indicating the presence of slitlike pores.[21] The quantitative values of the BET surface area, average pore size, and total pore volume are summarized in Table 1. The TiO$_2$ exhibited the highest BET surface area of 52.38 m^2/g and a total pore volume of 0.0629 cm^3/g, followed by CeO$_2$ (5.432 m^2/g), Nb$_2$O$_5$ (2.487 m^2/g), WO$_3$ (0.595 m^2/g), and Bi$_2$O$_3$ (0.141 m^2/g), respectively.

The optical absorption spectra of all utilized commercial semiconductors were also examined in the wavelength of 300−800 nm at room temperature. As displayed in Figure 3a, both TiO$_2$ and Nb$_2$O$_5$ displayed high absorbance at wavelengths lower than 380 nm and exhibited a very low intensity spectrum at wavelengths higher than 380 nm, indicating their visible light inertness. At an identical wavelength, CeO$_2$ showed a higher absorbance spectrum than TiO$_2$ and Nb$_2$O$_5$; however, it
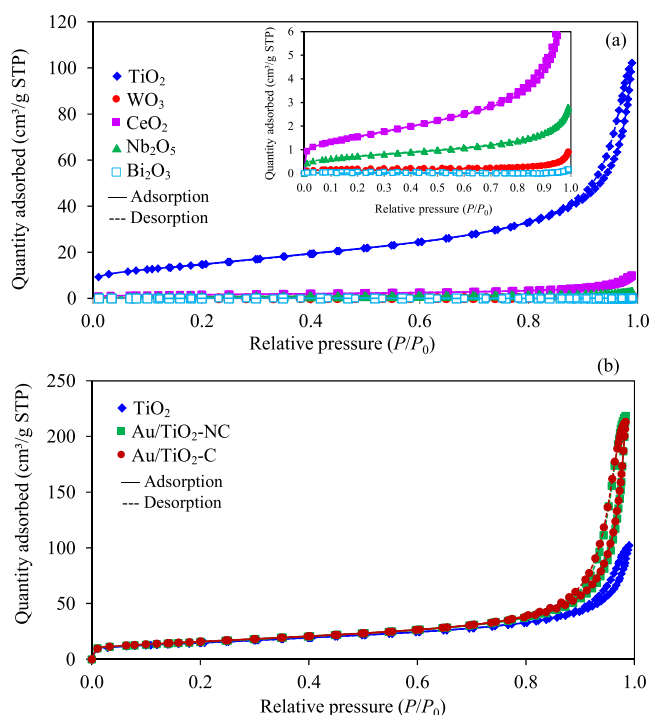
Figure 2. Representative N$_2$ adsorption/desorption isotherms of (a) commercial semiconductors and (b) Au/TiO$_2$ obtained from the photocatalytic recovery of Au from the simulated spent plating bath solution in the absence and presence of complexing agents at a semiconductor loading of 4 g/L and a light intensity of 4.1 mW/cm^2.
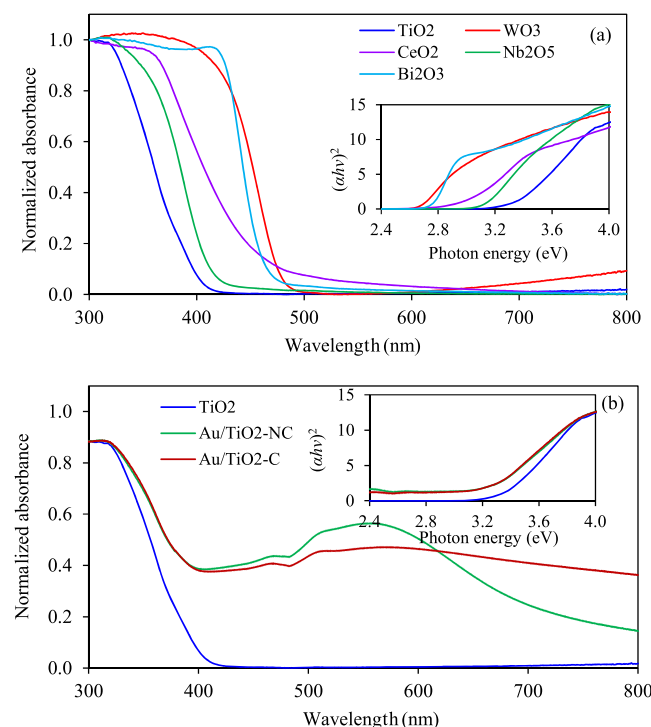
Figure 3. Representative UV−vis spectra of (a) commercial semiconductors and (b) Au/TiO$_2$ obtained from the photocatalytic recovery of Au from the simulated spent plating bath solution in the absence and presence of complexing agents at a semiconductor loading of 4 g/L and a light intensity of 4.1 mW/cm^2 and their Tauc plots (inset figure).

was still active in the UV region. Either WO_3 or Bi_2O_3 clearly exhibited a larger red shift in the absorbance spectra than other utilized semiconductors up to a wavelength of 480 nm, suggesting their ability to absorb both UV light and the short-wavelength visible light. The optical band gap energy (E_g) of all employed semiconductors was quantitatively determined via the Tauc plot according to eq 1.[22]

$$(\alpha h\nu)^{1/n} = A(h\nu - E_g) \qquad (1)$$

where α is the optical absorption coefficient, $h\nu$ is the photon energy, and A is the proportionality constant. In this equation, n is related to the type of optical transition process in semiconductors ($n = 1/2$ and 2 for the direct and indirect band gap semiconductors, respectively).

The band gap values of all utilized semiconductors were obtained from the x-intercept of the plot of $(\alpha h\nu)^2$ against the photon energy (inset of Figure 3a) and are listed in Table 1. The values of the band gap energy of all utilized semi-conductors can be ranked in the order $TiO_2 > Nb_2O_5 > CeO_2 > Bi_2O_3 > WO_3$, indicating the reverse trend of the visible light absorption ability.

2.2. Photocatalytic Recovery of Au from the Simulated Spent Non-Cyanide Plating Bath Solution.

2.2.1. Effect of Semiconductor Types.
The photocatalytic recovery of Au from the simulated spent plating bath solution at a pH of 3.2 by commercial semiconductors at a loading of 4 g/L and a light intensity of 4.1 mW/cm² is shown in Figure 4.
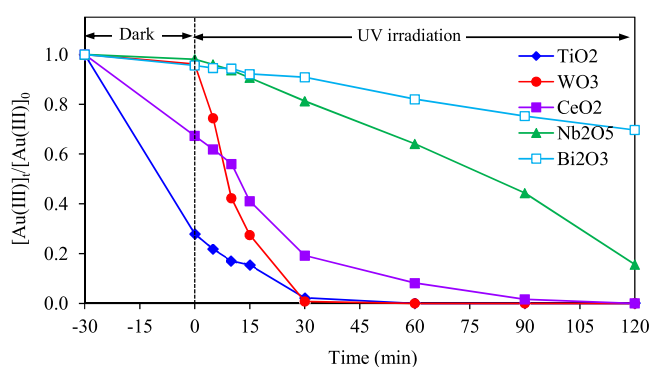
Figure 4. Photocatalytic recovery of Au from the simulated spent plating bath solution at a pH of 3.2 by commercial semiconductors at a loading of 4 g/L and a light intensity of 4.1 mW/cm².

Under the dark condition, approximately 72 and 33% of Au ions were adsorbed in the presence of TiO_2 and CeO_2, while only 2−4% of Au ions were adsorbed in the presence of WO_3, Nb_2O_5, and Bi_2O_3. This indicated the highest adsorption capacity of Au ions via TiO_2. Typically, the adsorption of some active substances on the surface of the adsorbent occurs via electrostatic interactions, which usually depend on the available surface area and surface charges of adsorbents.[23] A high adsorption of Au ions in the presence of TiO_2, followed by CeO_2, might be due to their high BET surface area and total pore volume available to adsorb some $AuCl_4^-$ species compared to other utilized semiconductors. In addition, the value of surface charges or point of zero charges (PZCs) of semiconductors is dependent on the solution pH. That is, when the solution pH is higher than the PZC value, the adsorbent usually exhibits negative surface charges and strongly prefers to adsorb cationic molecules. However, when the solution pH is lower than the PZC value, the

adsorbent demonstrates positive surface charges and favors the adsorption of anionic molecules.[24] In this case, the experimental PZC values of TiO_2, WO_3, CeO_2, Nb_2O_5, and Bi_2O_3 were ~6.6, ~5.6, ~6.4, ~6.2, and ~10.4, respectively. Thus, all utilized semiconductors displayed positive surface charges, which are able to adsorb the anionic charge of $AuCl_4^-$ in an acidic solution.[25]

Under the light irradiation, the Au ions were completely recovered within 30 min in the presence of either TiO_2 or WO_3 and within 120, 480, and 480 min in the presence of CeO_2, Nb_2O_5, and Bi_2O_3, respectively. TiO_2 displayed the highest rate of Au recovery even though it has the highest band gap energy (~3.35 eV), probably due to its highest adsorption capacity to the Au ions, which readily proceed to the reaction with the photogenerated e⁻ under the irradiated light. However, this is not the case with WO_3. Although it exhibited very low Au ion adsorption capacity, it displayed a very fast rate of Au recovery, probably attributed to its short band gap energy, which can harvest a high quantity of incident light to proceed to the photocatalytic reaction. This suggested that both textural and optical properties of semiconductors played an important role in the photocatalytic recovery of Au from the simulated spent solution.

2.2.2. Effect of Solution pH.
Typically, the Au ions can exist in different forms in a chloride solution depending on the solution pH. That is, at a pH below 6.2, the Au ions are dominantly found in the form of tetrachloroaurate ($AuCl_4^-$), while both $AuCl_4^-$ and hydroxylated gold chloride species [$AuCl_3(OH)^-$] are mainly found at a pH of 6.2−8.4. At a higher pH value (>8.4), the large hydroxylated gold chloride species are still dominant, starting from $AuCl_2(OH)_2^-$ to the others.[25] Figure 5 shows the effect of the initial pH on the photocatalytic recovery of Au from the simulated spent plating bath solution using the TiO_2 and WO_3 at a loading of 4 g/L
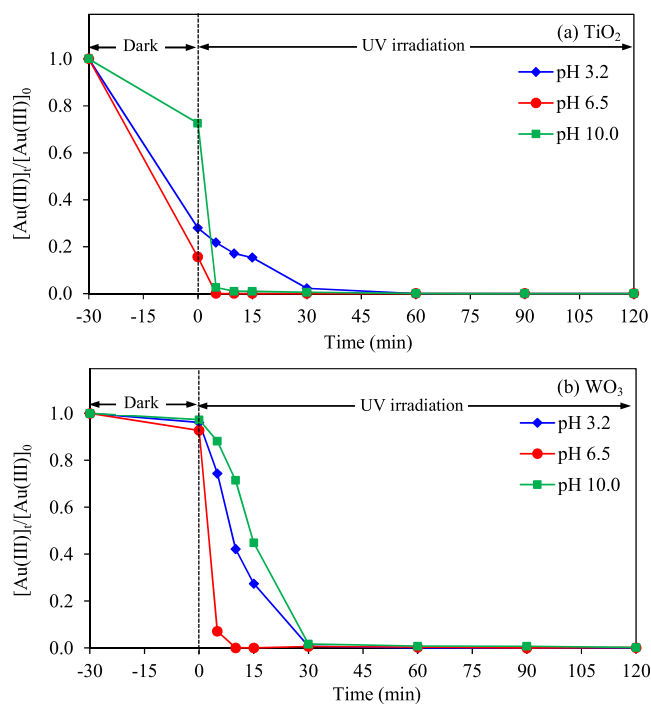
Figure 5. Effect of initial pH on the photocatalytic recovery of Au from the simulated spent plating bath solution via (a) TiO_2 and (b) WO_3 at a loading of 4 g/L and a light intensity of 4.1 mW/cm².

and a light intensity of 4.1 mW/cm^2. In the absence of light, approximately 72 and 84% of Au ions were adsorbed by TiO$_2$ at pH values of 3.2 and 6.5, respectively, but around 27% of Au ions were adsorbed at a pH of 10.0. However, approximately 3−7% of Au ions were adsorbed in the presence of WO$_3$ for all pH values. This is attributed to the synergetic effect of the PZC value and textural properties of both semiconductors. That is, the TiO$_2$ exhibited a high adsorption capacity under acidic conditions because it theoretically exhibits the positive surface charges as TiOH$_2^+$ species,[26] which can interact well with the negative charge of hydroxylated gold chloride species. However, in a basic solution, TiO$_2$ exhibited negative surface charges (as TiO$^-$),[26,27] which do not favor electrostatic interactions with the large hydroxylated gold chloride species such as AuCl$_2$(OH)$_2^-$. Therefore, the discrimination of Au ions in the basic environment is possibly caused by the preferential adsorption of Au at the pore surfaces of TiO$_2$ via the intermolecular cohesion forces. Low adsorption of Au ions in the presence of WO$_3$ might be due to its low surface area. In the presence of irradiated light, a fast reduction of Au ions was observed in the presence of TiO$_2$ at all pH values, likely due to the immediately photocatalytic reduction of adsorbed Au ions. In WO$_3$, although almost similar quantities of Au ions were adsorbed in a dark environment for all pH values, a fast decrease of Au ions was observed via the solution with a pH of 6.5. This might be due to an appropriate aggregation of WO$_3$ in the solution that has a pH value close to the PZC value, which can induce an effective transfer of e$^-$ and h$^+$ to the adjacent particles under a thorough stirring condition, resulting in a prolonged e$^-$–h$^+$ lifetime as well as an enhanced photocatalytic activity.[28] The sluggish reduction rate of Au ions in a strong basic solution (pH of 10.0) might be due to the steric hindrance of the large hydroxylated gold chloride molecules that competitively combined with the WO$_3$ to proceed with the photocatalytic reaction.

2.2.3. Effect of Complexing Agents. To produce smooth and ductile gold deposits with low stress and hardness as well as a good dimensional tolerance from a typical non-cyanide gold plating bath, two types of complexing agents, including sulfite (SO$_3^{2-}$) and thiosulfate (S$_2$O$_3^{2-}$), are usually added to promote the bath stability at a near-neutral pH.[29] Thus, the spent solution discharged from the plating unit usually contains a trace quantity of a residual sulfite−thiosulfate mixed agent. To investigate the effect of complexing agents on the photocatalytic recovery of Au from the simulated spent non-cyanide plating bath, two types of complexing agents were employed, including Na$_2$SO$_3$ and Na$_2$S$_2$O$_3$. Figure 6 shows the photocatalytic recovery of Au from the simulated spent plating bath solution at pH of 6.5 using TiO$_2$ and WO$_3$ at a loading of 4 g/L and a light intensity of 4.1 mW/cm^2 in the presence of complexing agents. It clearly demonstrated that the presence of both complexing agents affected the overall efficiency of the photocatalytic process. Under the dark condition, the presence of both complexing agents decreased the quantity of adsorbed Au ions on the surface of both semiconductors compared with that in the absence of complexing agents. A slightly high quantity of Au ions was adsorbed via TiO$_2$ in the presence of Na$_2$SO$_3$ compared with Na$_2$S$_2$O$_3$, while they did not adsorb via WO$_3$ in the presence of both complexing agents. This might be attributed to the effect of the available surface area of the employed semiconductors and the different forms of Au complex species in the presence of complexing agents. That is, the dominant Au species in the presence of Na$_2$SO$_3$ and
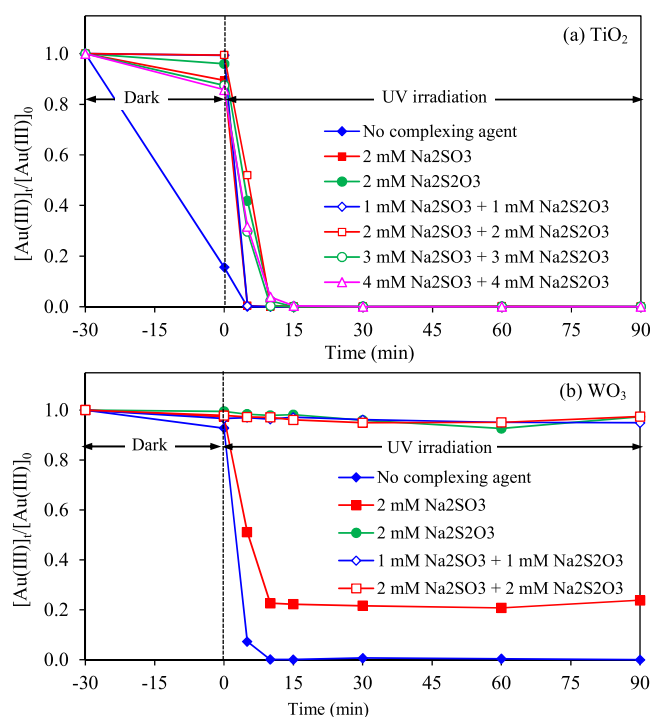
Figure 6. Effect of complexing agents on the photocatalytic recovery of Au from the simulated spent plating bath solution at pH of 6.5 via (a) TiO$_2$ and (b) WO$_3$ at a loading of 4 g/L and a light intensity of 4.1 mW/cm^2.

Na$_2$S$_2$O$_3$ are Au(SO$_3$)$_2^{3-}$ and Au(S$_2$O$_3$)$_2^{3-}$, respectively.[29] A low adsorption of Au(S$_2$O$_3$)$_2^{3-}$ on the surface of TiO$_2$ compared with Au(SO$_3$)$_2^{3-}$ was probably due to its large molecular size, which can hamper the adsorption by steric hindrance. In addition, the byproduct S$_2$O$_3^{2-}$ that can be generated during the adsorption of Au(S$_2$O$_3$)$_2^{3-}$ according to reaction R1[1] can obstruct further adsorption of Au(S$_2$O$_3$)$_2^{3-}$ on the adsorbent surface. A small quantity of both Au complex species was adsorbed on the surface of WO$_3$, presumably due to a very low surface area of WO$_3$.

$$2[\text{Au}(\text{S}_2\text{O}_3)_2]^{3-} \leftrightarrow (\text{Au}_2\text{S}_2\text{O}_3)_{ads} + 3\text{S}_2\text{O}_3^{2-} \qquad (R1)$$
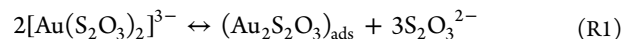
Under irradiated light, the presence of 2 mM Na$_2$SO$_3$ did not hinder the photocatalytic recovery of Au using TiO$_2$, and all Au ions were completely recovered within 5 min. However, it remarkably decreased the photocatalytic recovery of Au using WO$_3$, in which approximately 80% of Au ions were recovered within 90 min. The presence of 2 mM Na$_2$S$_2$O$_3$ slightly slowed down the photocatalytic recovery of Au using TiO$_2$, in which all Au ions were completely reduced within 10 min. However, it completely interrupted the photocatalytic recovery of Au using WO$_3$. This might be due to the synergetic effect of the low surface area of WO$_3$ and the molecular steric hindrance of Au(S$_2$O$_3$)$_2^{3-}$.

In the presence of both sulfite and thiosulfate at a pH value of 6.0−7.5, the dominant species of Au ions are reported in the form of sulfite and thiosulfate Au complexes as (Au$_2$S$_2$O$_3$)-(SO$_3$)$_2$.[1−5][1−5] As also demonstrated in Figure 6, neither adsorption nor photocatalytic reduction of Au was observed via WO$_3$ in the presence of mixed complexing agents for all utilized concentrations. Different concentrations of complexing agents exhibited different behaviors of Au ion adsorption in the TiO$_2$ system. That is, the adsorption of Au ions on the surface
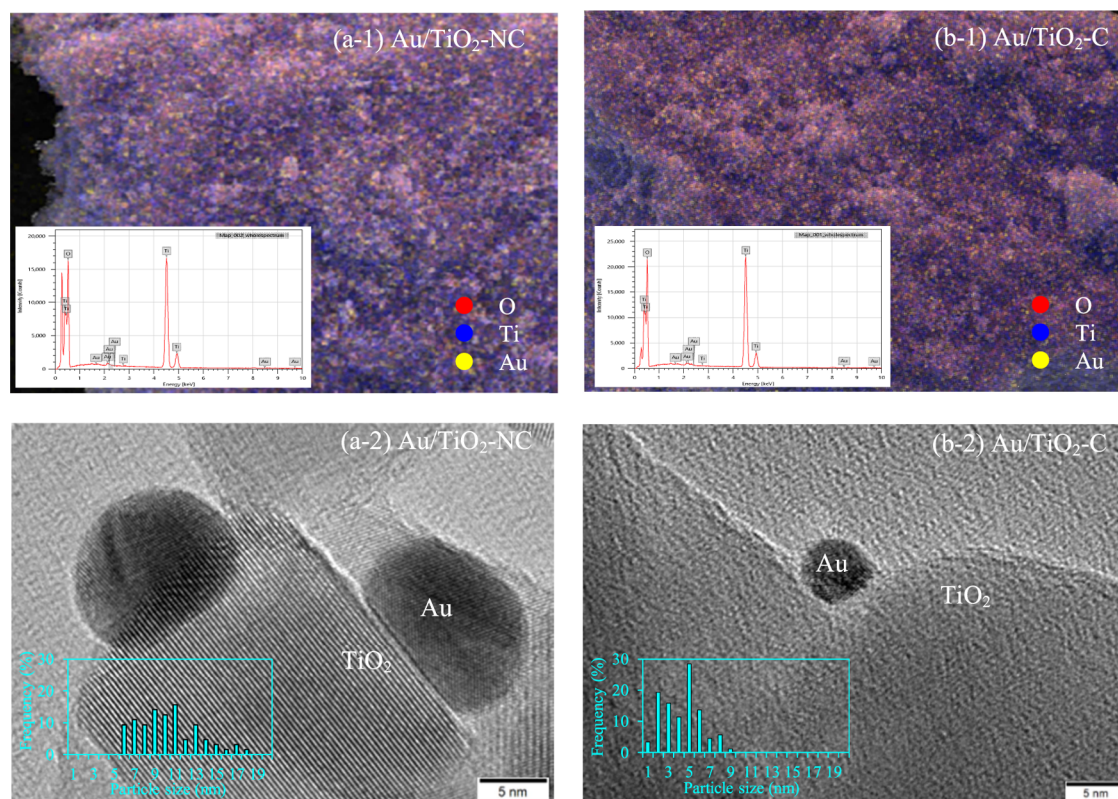
Figure 7. Representative SEM (1) and HRTEM (2) images of Au/TiO$_2$ obtained from the photocatalytic recovery of Au ions from the simulated spent plating bath solution in the (a) absence and (b) presence of complexing agents.

of TiO$_2$ was extremely low in the presence of low concentrations of mixed complexing agents (1 and 2 mM of each agent). Slightly higher adsorption can be achieved in the presence of high concentrations of mixed complexing agents (3 and 4 mM of each agent). This is probably because a high concentration of $(Au_2S_2O_3)(SO_3)_2^{5-}$ in the bulk liquid can initiate a high concentration gradient between the bulk phase and the surface of TiO$_2$, resulting in an increased mass transfer as well as an increased adsorption capacity.[30,31] In the presence of light, increasing the concentration of mixed complexing agents slightly decreased the photocatalytic efficiency for Au recovery compared with that in the absence of complexing agents, probably attributed to the shielding behavior of densely surrounded species in the presence of a high concentration of complexing agents. Based on the obtained results, among all employed commercial semiconductors, TiO$_2$ exhibited the highest photocatalytic recovery of Au from the simulated spent non-cyanide plating bath both in the absence and presence of complexing agents at all explored concentrations.

2.3. Morphology and Photocatalytic Activity of the Obtained Au/TiO$_2$. As reported elsewhere, the Au NP-decorated semiconductor exhibited an effective photocatalytic activity for various applications such as wastewater remediation,[32−36] hydrogen production from water splitting,[37,38] precious metal recovery,[19,39] glycerol conversion to value-added compounds,[40−42] etc. Thus, the morphology and photocatalytic activity of the Au/TiO$_2$ obtained from the simulated spent plating bath solution in the absence and presence of mixed complexing agents, denoted Au/TiO$_2$-NC and Au/TiO$_2$-C, respectively, were then explored.

As qualitatively shown in Figure 1b, both Au/TiO$_2$-NC and Au/TiO$_2$-C exhibited the main characteristic peaks of the

TiO$_2$-based material with comparable anatase content (Table 1), calculated according to the Spurr and Myers equations (eq 2).[43] No characteristic peaks of decorated Au were observed, probably because of their presence in good dispersion of small quantities or even in amorphous form. Thus, the SEM-EDX analysis was carried out to identify the presence of decorated Au on the surface of TiO$_2$. As displayed in Figure 7a-1,b-1, a good dispersion of Au was clearly observed with the entire loading of 1.37 ± 0.02 and 1.02 ± 0.03 wt % in Au/TiO$_2$-NC and Au/TiO$_2$-C, respectively (Table 1). On HRTEM analysis, the average particle size of Au in Au/TiO$_2$-C was significantly smaller than that in the Au/TiO$_2$-NC (Figure 7a-2,b-2). This is probably due to the effect of different forms of Au complex in the absence and presence of complexing agents during the photocatalytic process. That is, in the presence of sulfite−thiosulfate complexing agents, a large Au complex form such as $(Au_2S_2O_3)(SO_3)_2^{5-}$ generally forms.[1] This large Au complex might hinder the competitive adsorption and photocatalytic reduction of each other, higher than those in the absence of complexing agents, which in turn reduced the agglomeration of deposited Au NPs on the TiO$_2$ surface. As regards the textural property, both types of Au/TiO$_2$ still displayed H4-shaped hysteresis loops of the type IV isotherm with comparable textural properties (Figure 2b and Table 1), which were slightly better than those of pristine TiO$_2$. This is due to the good dispersion of Au NPs on the TiO$_2$ surface.[44]

$$x_A = \frac{100}{1 + [I_R/(0.8I_A)]} \tag{2}$$

where x_A is the anatase weight fraction, I_A is the relative reflection intensities of anatase, and I_R is the relative reflection intensities of rutile.

The absorption spectra of the Au/TiO$_2$ obtained from the photocatalytic recovery of Au from the simulated spent plating bath solution in the absence and presence of complexing agents were also explored in the range of 300−800 nm (Figure 3b). It can be observed that the Au/TiO$_2$ obtained from both conditions exhibited a red shift in absorption toward the wavelength longer than 400 nm, indicating the ability to absorb more incident visible light. The Au/TiO$_2$-NC revealed an intense broad band centered at a wavelength of 550 nm due to the oscillation and polarization of the excited electrons in the decorated Au structure called LSPR, which can effectively promote visible light absorption.[45] The Au/TiO$_2$-C exhibited unclear LSPR behavior in comparison with the Au/TiO$_2$-NC, probably due to the presence of too small particle sizes of Au NPs in its structure,[46] causing a low intensity of light absorption and scattering cross sections as well as the local electromagnetic field enhancement.[47] By applying Tauc's equation, the band gap energies of both Au/TiO$_2$ were comparable at 3.19−3.20 eV, which were lower than that of the TiO$_2$-based material.

The chemical state and bonding of Ti, O, and decorated Au were then examined by XPS analysis. The survey spectra clearly revealed the spectrum of O 1s, Ti 2p, and C 1s peaks of the O, Ti, and C (from carbon tape) (Figure 8). Using high-
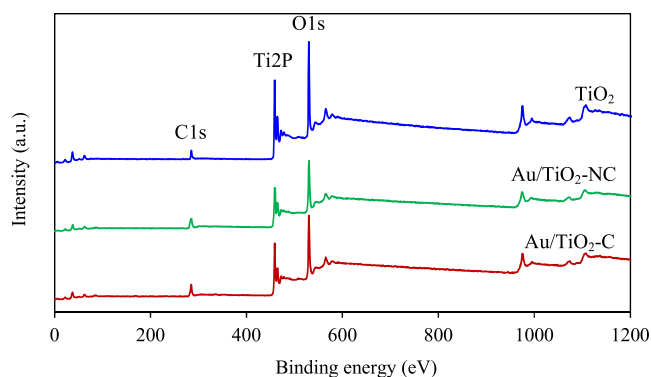
Figure 8. Representative survey XPS spectra of the TiO$_2$ and Au/TiO$_2$ obtained from the photocatalytic recovery of Au from the simulated spent plating bath solution in the absence and presence of complexing agents.

resolution XPS, the spectra of the pristine TiO$_2$ showed two symmetric peaks at binding energies of 464.1 and 458.4 eV (Figure 9a-1), corresponding to the Ti 2p$_{1/2}$ and Ti 2p$_{3/2}$ components of Ti^{4+}.[48−50] For the Au/TiO$_2$, the characteristic peaks of both Ti 2p components still appeared at the same binding energy compared with TiO$_2$. No satellite peaks at the low binding energy of both doublets were observed in both Au/TiO$_2$ (Figure 9b-1,c-1), indicating the absence of the Ti^{3+} state or the defective structure. The XPS spectra of asymmetric O 1s contained two symmetric peaks of the O$_2^-$ and OH$^-$ of the crystallite network at binding energies of ∼530.2 and ∼531.7 eV, respectively[51−53] (Figure 9a-2,b-2,c-2). The XPS spectra of Au revealed two principal peaks of Au 4f$_{5/2}$ and Au 4f$_{7/2}$ at binding energies of 86.7 and 83.1 eV with a spin−orbit splitting of 3.7 eV (Figure 9b-3,c-3), which is in good agreement with the values of the monometallic Au.[54] The presence of shoulder peaks with a higher binding energy for each Au 4f component was not observed, indicating the presence of monometallic Au on the TiO$_2$ surface.[41,54] At low binding energy, the XPS spectra of TiO$_2$, Au/TiO$_2$-NC, and

Au/TiO$_2$-C, respectively, displayed maximum binding energies of around 2.74, 1.70, and 1.40 eV (Figure 10a), indicating a negative shift of the VB edge of TiO$_2$ in the presence of decorated Au NPs. According to the obtained VB edges of all samples, the minimum conduction band (CB) of the respective samples would occur at −0.61, −1.50, and −1.79 eV. Therefore, the band positions of all samples are roughly sketched in Figure 10b.

Figure 11 illustrates the photocatalytic activity of the obtained Au/TiO$_2$ samples through two photocatalytic processes under UV−vis light. It can be seen that both Au/TiO$_2$-NC and Au/TiO$_2$-C exhibited comparable photocatalytic activity for MB degradation under UV−vis light. Approximately 80% of MB was degraded within 180 min, which was lower than that of TiO$_2$, in which around 88% of MB was degraded at the same reaction time (Figure 11a). According to the nature of the photocatalytic process, when the semiconductor or photocatalyst (S) absorbs the irradiated light that has the photon energy higher than its band gap energy, the electron (e$^-$) will be excited from the VB to the CB, leaving the hole (h$^+$) at the VB, as shown in reaction R2.[55,56] The photogenerated h$^+$ can react with the adsorbed water (H$_2$O) to form hydroxyl radicals (HO$^\bullet$) and proton (H$^+$) (reaction R3), while the photoexcited e$^-$ at the CB can react with the dissolved oxygen (O$_2$) to form the superoxide radicals (O$_2^{\bullet-}$) (reaction R4). Both HO$^\bullet$ and O$_2^{\bullet-}$ generated are the reactive oxidizing species, which can attach and degrade the MB molecules according to reaction R5.[56]

$$S + h\nu \; (\text{UV} - \text{vis light}) \rightarrow S^* \; (e^- + h^+) \tag{R2}$$

$$H_2O + h^+ \rightarrow HO^\bullet + H^+ \tag{R3}$$

$$O_2 + e^- \rightarrow O_2^{\bullet-} \tag{R4}$$

$$MB + (HO^\bullet, h^+, O_2^{\bullet-}) \rightarrow \text{degraded products} \tag{R5}$$
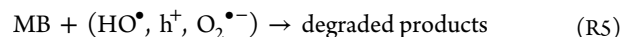
where S* is the S in the excited state.

The low photocatalytic activity of MB degradation in the presence of Au/TiO$_2$ in comparison with the TiO$_2$ might be attributed to their less-positive VB edge to produce HO$^\bullet$ (Figure 10b). Thus, the degradation of MB in the presence of Au/TiO$_2$ is mainly dominated by the h$^+$ or O$_2^{\bullet-}$ and not HO$^\bullet$ as usual.[57] The photocatalytic degradation of MB via all employed photocatalysts was then fitted with the Langmuir−Hinshelwood model, as expressed in eq 3.[33]

$$C/C_0 = \exp(-kt) \tag{3}$$

where C_0 is the initial concentration of the substance, C is the concentration of the substance at a particular time t, and k is the first-order reaction rate constant.

As tabulated in Table 2, the apparent rate constants for MB degradation in the presence of Au/TiO$_2$-NC and Au/TiO$_2$-C were found to be 0.0080 and 0.0085 min^{-1}, which were lower than that of the pristine TiO$_2$ for 1.38- and 1.30-fold, respectively. Compared with the literature, the Au/TiO$_2$ prepared from the proposed method gave a rate constant comparable to that of Au/TiO$_2$ prepared by the sol−gel method ($k \sim 0.0067$ min^{-1})[58] but lower than that of the TiAu1 prepared by the incipient wetness method ($k \sim 0.0687$ min^{-1})[57] or TiO$_2$−1%Co−2.5%Fe prepared by the solvothermal method ($k \sim 0.0186$ min^{-1}).[59]

Regardless of the photocatalytic reduction of Au from the actual spent cyanide plating bath solution, approximately 3% of
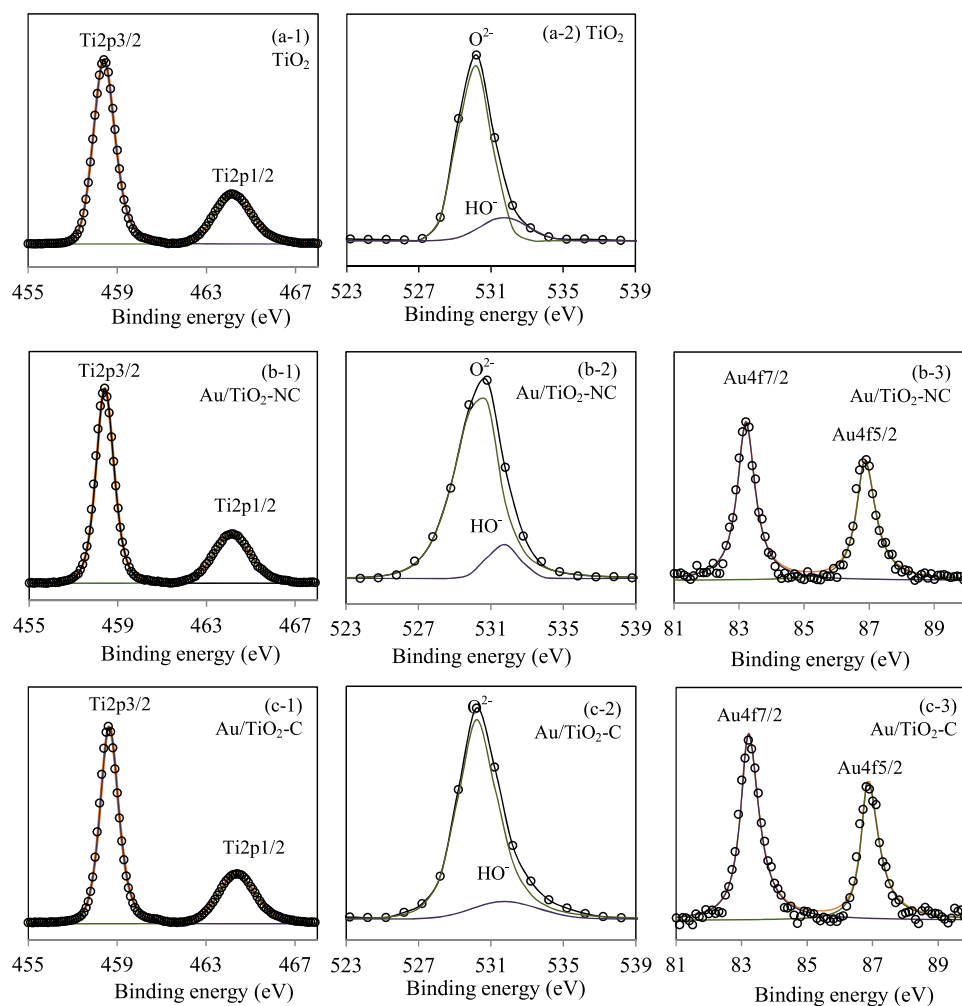
Figure 9. (a) Representative HR-XPS spectra of the (1) Ti 2p, (2) O 1s, and (3) Au 4f of (a) TiO_2, (b) Au/TiO_2-NC, and (c) Au/TiO_2-C.

$Au(CN)_2^-$ was reduced during the reaction time of 2 h using pristine TiO_2 as the photocatalyst (Figure 11b). However, approximately 77 and 24% of $Au(CN)_2^-$ were reduced using Au/TiO_2-NC and Au/TiO_2-C as photocatalysts, respectively. Typically, in the oxygenated system, the reduction reaction of $Au(CN)_2^-$ to Au via the photogenerated e^- occurs at the VB (reaction R6) at a reduction potential of around -0.57 V/ NHE.[60] Moreover, the dissolved O_2 can competitively react with the photogenerated e^- to form H_2O_2 at a slightly low reaction potential (-0.146 V/NHE) according to reaction R7.[61] The generated H_2O_2 can dissociate in the presence of the incident light or react with the photogenerated e^- to form $HO^\bullet$ radicals (reactions R8). Meanwhile, the formed CN^- ions are readily oxidized by the photogenerated h^+ and/or $HO^\bullet$ at VB to form CNO^- according to reactions R9 and R10.[8,61]

$$Au(CN)_2^- + e^- \rightarrow Au + 2CN^- \tag{R6}$$

$$O_2 + 2e^- + 2H_2O \rightarrow H_2O_2 + 2OH^- \tag{R7}$$

$$H_2O_2 + H^+ + e^- \rightarrow 2HO^\bullet + HO^- \tag{R8}$$

$$CN^- + 2h^+ + 2OH^- \rightarrow CNO^- + H_2O \tag{R9}$$

$$CN^- + HO^\bullet \rightarrow CNO^- \tag{R10}$$
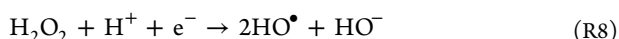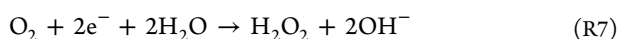
According to the sketched band position (Figure 10b), both TiO_2 and Au/TiO_2 samples exhibited a more negative CB level

than the reduction potential of $Au(CN)_2^-$, indicating their ability to reduce $Au(CN)_2^-$ to Au from the spent cyanide plating bath solution. A lack of photocatalytic reduction of $Au(CN)_2^-$ via TiO_2 during the reaction time of 2 h was probably due to a competitive reaction of dissolved O_2 with the photoexcited e^-, resulting in a low quantity of remaining e^- to react with the $Au(CN)_2^-$. As the reaction proceeded, a massive amount of dissolved O_2 was gradually consumed, and the deposition of Au over the surface of TiO_2 could be started. These Au clusters can act as an electron sink to trap the migrated e^-, which can prolong the lifetime of $e^- - h^+$ pairs as well as increase the photocatalytic efficiency.[62-64] The photocatalytic reduction of $Au(CN)_2^-$ via TiO_2 was previously observed at around 75% when the reaction time was extended to 8 h (data not shown). This is not for the case of Au/TiO_2 samples in which a faster photocatalytic reduction of $Au(CN)_2^-$ was observed. This might be due to a combined effect between the presence of Au NPs that acted as the electron sink during the reaction, which can improve the charge transfer rate and decrease the band gap energy of both Au/TiO_2 samples compared with TiO_2, effectively harvesting the incident light to drive the excitation of e^- from the VB to the CB to perform the photocatalytic reduction. The Au/TiO_2-C exhibited slightly lower activity to reduce $Au(CN)_2^-$ than the Au/TiO_2-NC, due to its lower LSPR behavior. Using the Langmuir–Hinshelwood model, the Au/TiO_2-NC exhibited
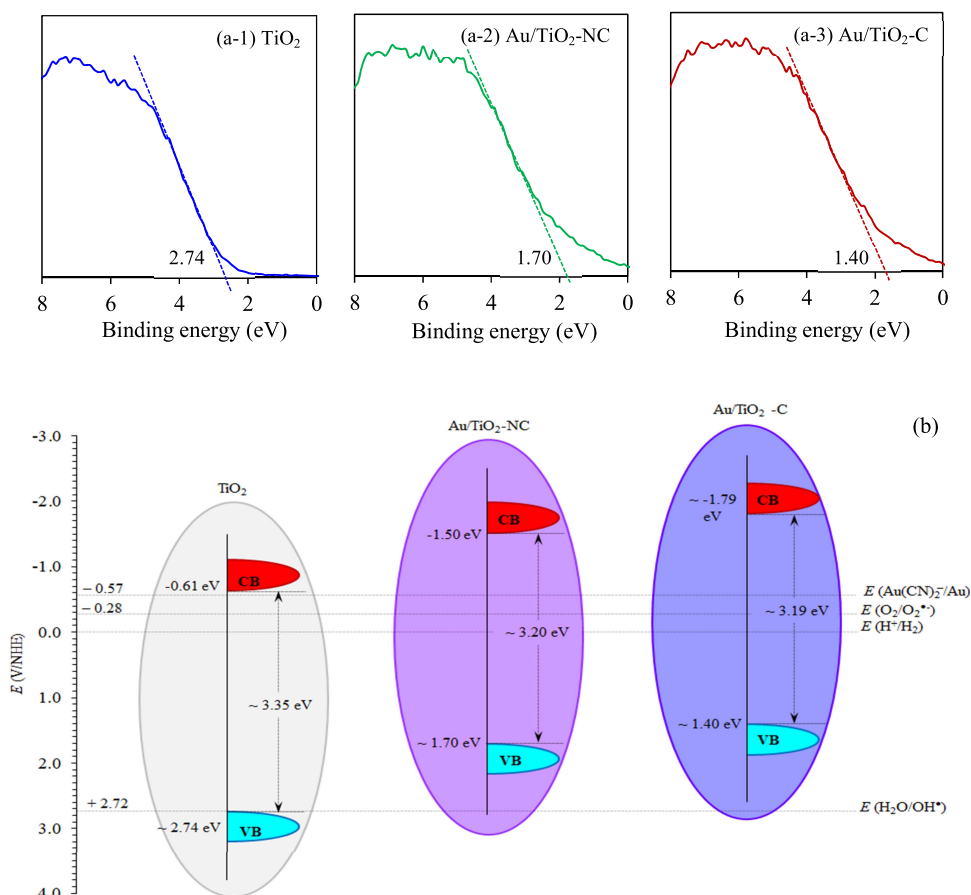
Figure 10. (a) Representative XPS spectra of (1) TiO_2, (2) Au/TiO_2-NC, and (3) Au/TiO_2-C photocatalysts at low binding energy and (b) scheme of their band position.
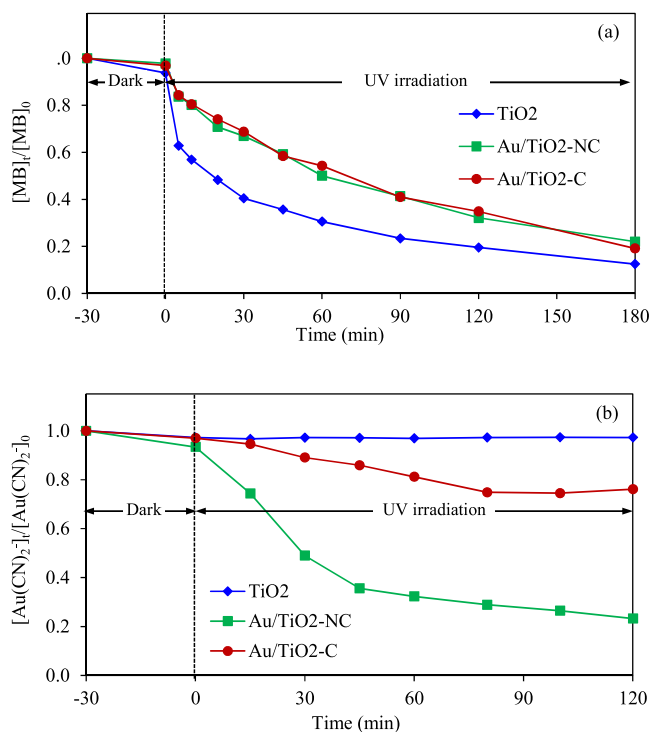
Figure 11. Photocatalytic activity of the obtained Au/TiO_2 via (a) MB degradation and (b) Au recovery from the actual spent cyanide plating bath solution.

Table 2. Apparent Reaction Rate Constants for the Photocatalytic Activity of TiO_2 and Au/TiO_2

photocatalyst	MB degradation		Au recovery	
	k (min^{-1})	R^2	k (min^{-1})	R^2
TiO_2	0.0110	0.9274	0.0005	0.9516
Au/TiO_2-NC	0.0080	0.9760	0.0234	0.9982
Au/TiO_2-C	0.0085	0.9865	0.0035	0.9988

apparent rate constants for $Au(CN)_2^-$ recovery of 0.0234 min^{-1}, which was higher than those for TiO_2 and Au/TiO_2-C of around 46.8- and 7.0-fold, respectively (Table 2).

Based on the obtained results, although the Au/TiO_2-C exhibited a photocatalytic recovery of Au from the actual spent cyanide plating bath solution lower than that of Au/TiO_2-NC, it displayed the photocatalytic activity higher than that of pristine TiO_2 of around 25% at 2 h. The repetitive photocatalytic recovery of Au from the actual spent cyanide plating bath solution was then studied using the obtained Au/TiO_2-C as the original photocatalyst. Briefly, after the first experiment, the solid NPs were separated from the plating bath solution by centrifugation at 11 000 rpm, washed thoroughly with deionized water, dried at 80 °C for 3 h, and then subjected to the second experiment, and this was repeated. As displayed in Figure 12a, the quantity of decorated Au on the TiO_2-based material increased with increasing photocatalytic cycles. Moreover, the Au/TiO_2 obtained at a particular cycle can enhance the fast dwindling of $Au(CN)_2^-$ from the cyanide plating bath solution in the next cycle, probably due to a high
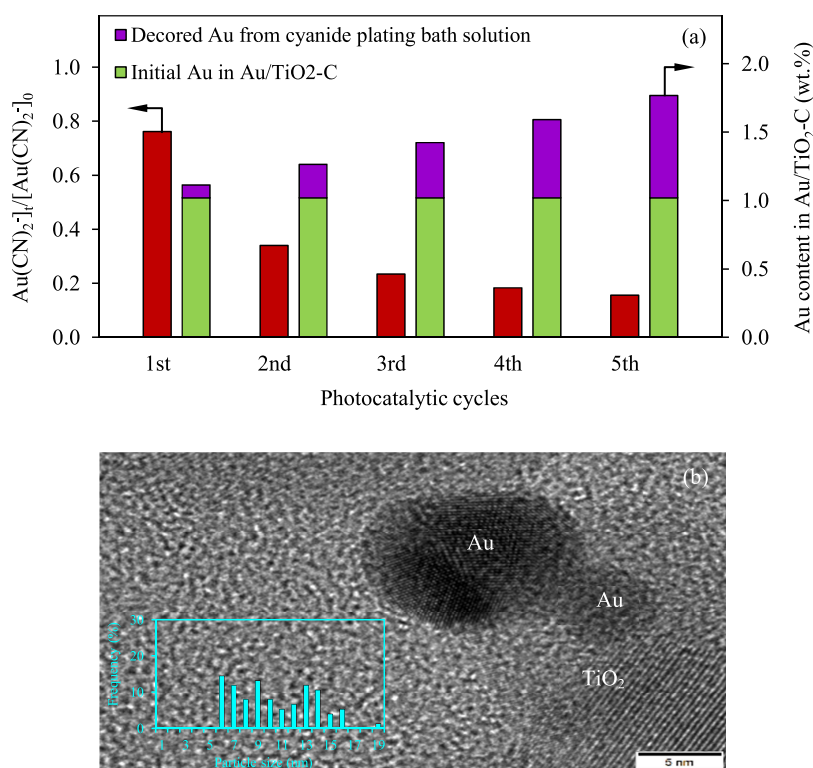
Figure 12. (a) Repetitive photocatalytic recovery of Au from the actual spent cyanide plating bath solution by the obtained Au/TiO$_2$-C at 120 min and (b) the particle size distribution after the fifth cycle.

LSPR behavior in the presence of high Au content in the Au/TiO$_2$ NPs.[45] After the fifth cycle, the size of decorated Au NPs was distributed in the range of 6−19 nm with an average value of 10.39 ± 3.28 nm (Figure 12b). The deposited Au NPs can simply separate from the TiO$_2$-based material using selective dissolution via a commercial chemical such as Aqua regia.[8]

According to the nature of the proposed application of the obtained Au/TiO$_2$-C for the Au recovery from the actual cyanide plating bath solution, the properties of the obtained Au/TiO$_2$ at each photocatalytic cycle changed accordingly due to the accumulation of decorated Au. Thus, the stability of the employed photocatalyst was examined from the phase change of the TiO$_2$-based material. As shown in Figure 13, the XRD pattern of the Au/TiO$_2$ obtained at the fifth cycle (Au/TiO$_2$-C(5)) still maintained the main characteristic peaks of the TiO$_2$-based material. The Au/TiO$_2$-C(5) NPs were found to
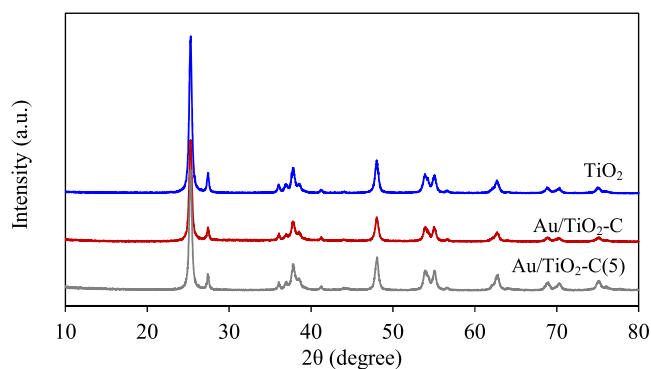
exhibit almost similar anatase contents (∼84.86%) compared to the Au/TiO$_2$-C NPs (∼84.28%), suggesting their stability after the fifth use.

3. CONCLUSIONS

Among all employed semiconductors, the photocatalytic recovery of Au from the simulated non-cyanide plating bath solution was accomplished well using the commercial TiO$_2$ as the photocatalyst at a loading of 4 g/L and pH of 6.5 because of its high surface area. The presence of either Na$_2$S$_2$O$_3$ or Na$_2$SO$_3$ at the concentrations of 1−4 mM insignificantly affected the photocatalytic recovery of Au. The Au was completely recovered within 5 and 15 min in the absence and presence of mixed complexing agents for all investigated concentrations. However, the presence of complexing agents remarkably affected the morphology of obtained Au/TiO$_2$ samples as well as the LSPR behavior. That is, the Au/TiO$_2$-C exhibited LSPR behavior lower than the Au/TiO$_2$-NC with a negative shift of the VB edge position. Regardless of the photocatalytic activity, both Au/TiO$_2$ samples exhibited poor photocatalytic activity for MB degradation in comparison with TiO$_2$ due to their less-positive VB position to produce the HO$^\bullet$ radicals. However, both Au/TiO$_2$ samples exhibited a higher photocatalytic activity to recover Au from the spent cyanide plating bath solution than TiO$_2$. This is because the deposited Au clusters promote the red shift of light absorption of TiO$_2$ as well as LSPR behavior. The Au/TiO$_2$-C exhibited an anatase content comparable to that of the TiO$_2$-based material after the fifth photocatalytic cycle of Au recovery from the actual cyanide plating bath solution.

Figure 13. Representative XRD patterns of the Au/TiO$_2$-C before and after the fifth use (Au/TiO$_2$-C(5)) for Au recovery from the cyanide plating bath solution.

4. MATERIALS AND METHODS

4.1. Chemicals. All chemicals employed in this work were analytical grade, including chloroauric acid (99.9% HAuCl$_4$·3H$_2$O; Sigma-Aldrich), sodium hydroxide (NaOH; Sigma-Aldrich), sodium thiosulfate (99.5% Na$_2$S$_2$O$_3$·5H$_2$O; Kemaus), and sodium sulfite (98% Na$_2$SO$_3$; Kemaus). Five commercial semiconductors were utilized as photocatalysts, including titanium dioxide (TiO$_2$; 99.5%, Sigma-Aldrich), tungsten(VI) oxide (WO$_3$; 99.9%, Sigma-Aldrich), niobium(V) oxide (Nb$_2$O$_5$; 99.99%, Sigma-Aldrich), cerium(IV) oxide (CeO$_2$; 99.995%, Sigma-Aldrich), and bismuth(III) oxide (Bi$_2$O$_3$; 99.999%, Sigma-Aldrich).

4.2. Photocatalytic Recovery of Au from the Simulated Spent Non-Cyanide Plating Bath Solution. The photocatalytic recovery of Au from the simulated spent non-cyanide plating bath solution was tested via several types of commercial semiconductors at an identical loading under UV−vis light irradiation. In each experiment, approximately 1.2 g of the respective semiconductors was dispersed in 300 mL of the simulated spent plating bath solution and filled in a 400 mL double-wall cylindrical glass reactor, which was then placed in the middle of the UV-protected box at the right position to receive the irradiated light. Afterward, the solution was agitated continuously with a magnetic stirrer at a constant rate of 400 rpm in the absence of light for 30 min to provide a good dispersion and equilibrium adsorption of Au ions on the surface of the semiconductor. After the equilibration period, the system was irradiated with the UV−vis light (100−600 nm) generated by a high-pressure mercury lamp (120 W; RUV 533 BC, Holland) at a light intensity of 4.1 mW/cm^2. The temperature of the photoreactor was precisely controlled at around 32 °C using the water circulation system as the reactor jacket. As the time proceeded, approximately 5 mL of the solution was sampled and centrifuged at 11 000 rpm (5804R, Eppendorf) to separate the solid portion from the aqueous mixture, and then the remaining Au ions were analyzed by flame atomic absorption spectrometry (Flame-AAS, AAnalyst 200+ flas 400; PerkinElmer). The amount of recovered Au from the simulated spent plating bath solution could be obtained by subtracting the initial concentration of Au ions with the unrecovered one. The results reported here are the average value of three repetitive experiments, and the acceptable error in this work was not greater than 3%.

4.3. Characterizations. The light absorption capacity and the diffuse reflectance spectra over the wavelength range of 300−800 nm were measured by ultraviolet−visible−near-infrared spectrophotometry (UV−vis; Lambda 950, PerkinElmer). The crystallite structure of all semiconductors was analyzed by X-ray diffractometry (XRD; D2 Phaser, Bruker). The surface morphology and chemical composition of the fresh semiconductors and Au-decorated semiconductors were primarily observed via scanning electron microscopy (SEM; JSM-IT-500HR, JEOL) with energy-dispersive X-ray spectrometry (EDX; JED-2300, JEOL) and high-resolution transmission electron microscopy (HRTEM; JEM-3100F, JEOL) with an accelerating voltage of 300 kV. The surface area, average pore size, and total pore volume were examined using a Multipoint Surface Area Analyzer (Tristar II3020, Micromeritics) via the Brunauer−Emmett−Teller (BET) method. The bonding and chemical state of the elements were determined with an X-ray photoelectron spectrometer (XPS; Axis Supra, Kratos, U.K.) with a Delay Line detector (DLD)

and a monochromatic Al Kα ($h\nu$ = 1486.6 eV) source. Accurate binding energies ($\pm$0.1 eV) were established with respect to the position of the adventitious carbon C 1s peak at 284.8 eV.

4.4. Photocatalytic Activity of the Obtained Au NP-Decorated Semiconductors. The photocatalytic activity of the Au NP-decorated semiconductors was examined with two photocatalytic processes, including the MB degradation and the Au recovery from the actual spent cyanide plating bath solution. The experimental setup of the MB degradation was similar to that in Section 2.2. In each experiment, approximately 200 mL of MB solution (50 mg/L, pH 7.58) with a photocatalyst loading of 0.25 g/L was first stirred at 300 rpm in the dark condition for 30 min and then irradiated by UV−vis light (100−600 nm) at a light intensity of 4.1 mW/cm^2. As the reaction proceeded, approximately 2.5 mL of MB solution was collected at a particular time and centrifuged at 11 000 rpm (5804R, Eppendorf) to separate the solid particles from the solution. Finally, the remaining MB concentration was quantitatively determined by measuring the absorbance at 664 nm using a UV−vis spectrophotometer (UV-1800, Shimadzu).

The Au recovery from the actual spent cyanide plating bath solution was determined using a similar experimental setup with the KAu(CN)$_2$ as the Au precursor at a photocatalyst loading of 4 g/L. The spent solution had a pH of 8.8−9.0 and contained Au ions of around 6.55 $\pm$ 0.12 mg/L and a trace quantity of iron (Fe), nickel (Ni), zinc (Zn), and copper (Cu) at concentrations less than 0.14, 0.99, 0.40, and 0.18 mg/L, respectively. The remaining concentration of Au ions in the spent solution was measured along the reaction times by flame atomic absorption spectrometry (Flame-AAS, AAnalyst 200+ flas 400; PerkinElmer).

■ AUTHOR INFORMATION

Corresponding Author

    Mali Hunsom − *Department of Chemical Engineering, Faculty of Engineering, Mahidol University, Nakhon Pathom 73170, Thailand; Associate Fellow of Royal Society of Thailand (AFRST), Bangkok 10300, Thailand;* ● orcid.org/0000-0002-4434-5276; Email: mali.hun@mahidol.edu

Authors

    Naphaphan Kunthakudee − *Department of Chemical Engineering, Faculty of Engineering, Mahidol University, Nakhon Pathom 73170, Thailand*

    Tarawipa Puangpetch − *Department of Chemical Engineering, Faculty of Engineering and Industrial Technology, Silpakorn University, Nakhon Pathom 73000, Thailand*

    Prakorn Ramakul − *Department of Chemical Engineering, Faculty of Engineering and Industrial Technology, Silpakorn University, Nakhon Pathom 73000, Thailand*

Complete contact information is available at:
https://pubs.acs.org/10.1021/acsomega.1c06362

Notes

The authors declare no competing financial interest.

Chemical Engineering, Faculty of Engineering, Mahidol University, for facilities and equipment support.

■ REFERENCES

(1) Kato, M.; Okinaka, Y. Some recent developments in non-cyanide gold plating for electronics applications. *Gold Bull.* **2004**, *37*, 37−44.

(2) Wang, Y.; Liu, H.; Bi, S.; He, M.; Wang, C.; Cao, L. Effects of organic additives on the immersion gold depositing from a sulfite−thiosulfate solution in an electroless nickel immersion gold process. *RSC Adv.* **2016**, *6*, 9656−9662.

(3) Yongpisanphob, W. *Industry Outlook 2021-2023: Electronics*; Krungsri Research, 2021.

(4) Green, T. A. Gold electrodeposition for microelectronic, optoelectronic and microsystem applications. *Gold Bull.* **2007**, *40*, 105−114.

(5) Rakhila, Y.; Elmchaouri, A.; Mestari, A.; Korili, S.; Abouri, M.; Gil, A. Adsorption recovery of Ag (I) and Au (III) from an electronics industry wastewater on a clay mineral composite. *Int. J. Miner., Metall. Mater.* **2019**, *26*, 673−680.

(6) Wahyuni, E.T.; Kuncaka, A.; Sutarno, S. Application of photocatalytic reduction method with TiO2 for gold recovery. *Am. J. Appl. Chem.* **2015**, *3*, 207−211.

(7) Wang, C.-y.; Liu, C.-y.; Zheng, X.; Chen, J.; Shen, T. The surface chemistry of hybrid nanometer-sized particles I. Photochemical deposition of gold on ultrafine TiO₂ particles. *Colloids Surf., A* **1998**, *131*, 271−280.

(8) van Grieken, R.; Aguado, J.; López-Muñoz, M.-J.; Marugán, J. Photocatalytic gold recovery from spent cyanide plating bath solutions. *Gold Bull.* **2005**, *38*, 180−187.

(9) Jalalah, M.; Faisal, M.; Bouzid, H.; Ismail, A. A.; Al-Sayari, S. A. Dielectric and photocatalytic properties of sulfur doped TiO₂ nanoparticles prepared by ball milling. *Mater. Res. Bull.* **2013**, *48*, 3351−3356.

(10) Fajrina, N.; Tahir, M. A critical review in strategies to improve photocatalytic water splitting towards hydrogen production. *Int. J. Hydrogen Energy* **2019**, *44*, 540−577.

(11) Zhang, F.; Wang, X.; Liu, H.; Liu, C.; Wan, Y.; Long, Y.; Cai, Z. Recent advances and applications of semiconductor photocatalytic technology. *Appl. Sci.* **2019**, *9*, 2489.

(12) Li, X.; Zhao, H.; Liang, J.; Luo, Y.; Chen, G.; Shi, X.; Lu, S.; Gao, S.; Hu, J.; Liu, Q.; Sun, X. A-site perovskite oxides: an emerging functional material for electrocatalysis and photocatalysis. *J. Mater. Chem. A* **2021**, *9*, 6650−6670.

(13) Avid, S. P. Tech Note: Removal of Heavy Metals by Photocatalyst. *Rev. Ing. UC* **2019**, *26*, 378−385.

(14) Kida, T.; Oshima, R.; Nonaka, K.; Shimanoe, K.; Nagano, M. Photoinduced recovery of gold using an inorganic/organic hybrid photocatalyst. *J. Phys. Chem. C* **2009**, *113*, 19986−19993.

(15) Wahyuni, E.; Aprilita, N.; Hatimah, H.; Wulandari, A.; Mudasir, M. Removal of toxic metal ions in water by photocatalytic method. *Am. Chem. Sci. J.* **2015**, *5*, 194−201.

(16) Kim, K. R.; Choi, S.; Yavuz, C. T.; Nam, Y. S. Direct Z-Scheme Tannin−TiO₂ Heterostructure for Photocatalytic Gold Ion Recovery from Electronic Waste. *ACS Sustainable Chem. Eng.* **2020**, *8*, 7359−7370.

(17) Vorobyova, T.; Poznyak, S.; Rimskaya, A.; Vrublevskaya, O. Electroless gold plating from a hypophosphite-dicyanoaurate bath. *Surf. Coat. Technol.* **2004**, *176*, 327−336.

(18) Kato, M.; Sato, J.; Otani, H.; Homma, T.; Okinaka, Y.; Osaka, T.; Yoshioka, O. Substrate (Ni)-Catalyzed Electroless Gold Deposition from a Noncyanide Bath Containing Thiosulfate and Sulfite: I. Reaction Mechanism. *J. Electrochem. Soc.* **2002**, *149*, C164.

(19) Chen, P.; Ni, J.; Liang, Y.; Yang, B.; Jia, F.; Song, S. Piezo-photocatalytic reduction of Au (I) by defect-rich MoS₂ nanoflowers for efficient gold recovery from a thiosulfate solution. *ACS Sustainable Chem. Eng.* **2021**, *9*, 589−598.

(20) Tahir, M. B.; Nabi, G.; Rafique, M.; Khalid, N.R. Technology, Nanostructured-based WO₃ photocatalysts: recent development, activity enhancement, perspectives and applications for wastewater treatment. *Int. J. Environ. Sci.* **2017**, *14*, 2519−2542.

(21) Xiang, Q.; Yu, J.; Jaroniec, M. Enhanced photocatalytic H₂-production activity of graphene-modified titania nanosheets. *Nanoscale* **2011**, *3*, 3670−3678.

(22) Makuła, P.; Pacia, M.; Macyk, W. How to correctly determine the band gap energy of modified semiconductor photocatalysts based on UV−Vis spectra. *J. Phys. Chem. Lett.* **2018**, *9*, 6814−6817.

(23) El Saliby, I.; McDonagh, A.; Erdei, L.; Shon, H. K. Water Reclamation by Heterogeneous Photocatalysis over Titanium Dioxide. In *Green Technologies for Sustainable Water Management*; American Society of Civil Engineers, 2016.

(24) Malato, S.; Fernández-Ibáñez, P.; Maldonado, M. I.; Blanco, J.; Gernjak, W. Decontamination and disinfection of water by solar photocatalysis: recent overview and trends. *Catal. Today* **2009**, *147*, 1−59.

(25) Agunloye, E.; Panariello, L.; Gavriilidis, A.; Mazzei, L. A model for the formation of gold nanoparticles in the citrate synthesis method. *Chem. Eng. Sci.* **2018**, *191*, 318−331.

(26) Shimura, K.; Yoshida, H. Heterogeneous photocatalytic hydrogen production from water and biomass derivatives. *Energy Environ. Sci.* **2011**, *4*, 2467−2481.

(27) Hoffmann, M. R.; Martin, S. T.; Choi, W.; Bahnemann, D. W. Environmental applications of semiconductor photocatalysis. *Chem. Rev.* **1995**, *95*, 69−96.

(28) Lakshminarasimhan, N.; Kim, W.; Choi, W. Effect of the agglomerated state on the photocatalytic hydrogen production with in situ agglomeration of colloidal TiO₂ nanoparticles. *J. Phys. Chem. C* **2008**, *112*, 20451−20457.

(29) Green, T.; Roy, S. Speciation analysis of Au (I) electroplating baths containing sulfite and thiosulfate. *J. Electrochem. Soc.* **2006**, *153*, C157.

(30) Kuboňová, L.; Obalová, L.; Vlach, O.; Troppová, I.; Kalousek, J. Modelling of NO adsorption in fixed bed on activated carbon. *Chem. Process Eng.* **2011**, *32*, 367−377.

(31) Ibrahim, H. G.; Al-Meshragi, M. A. Experimental Study of Adsorption on Activated Carbon for CO₂ Capture. In *CO₂ Sequestration*; IntechOpen, 2019.

(32) Orooji, Y.; Tanhaei, B.; Ayati, A.; Tabrizi, S. H.; Alizadeh, M.; Bamoharram, F. F.; Karimi, F.; Salmanpour, S.; Rouhi, J.; Afshar, S.; et al. Heterogeneous UV-Switchable Au nanoparticles decorated tungstophosphoric acid/TiO₂ for efficient photocatalytic degradation process. *Chemosphere* **2021**, *281*, No. 130795.

(33) Martins, P.; Kappert, S.; Nga Le, H.; Sebastian, V.; Kühn, K.; Alves, M.; Pereira, L.; Cuniberti, G.; Melle-Franco, M.; Lanceros-Méndez, S. Enhanced photocatalytic activity of Au/TiO₂ nano-particles against ciprofloxacin. *Catalysts* **2020**, *10*, 234.

(34) Do, T. C. M. V.; Nguyen, D. Q.; Nguyen, K. T.; Le, P. H. TiO₂ and Au-TiO₂ nanomaterials for rapid photocatalytic degradation of antibiotic residues in aquaculture wastewater. *Materials* **2019**, *12*, 2434.

(35) Zhang, L.; Liang, J.; Yue, L.; Xu, Z.; Dong, K.; Liu, Q.; Luo, Y.; Li, T.; Cheng, X.; Cui, G.; et al. N-doped carbon nanotubes supported CoSe₂ nanoparticles: A highly efficient and stable catalyst for H₂O₂ electrosynthesis in acidic media. *Nano Res.* **2022**, *15*, 304−309.

(36) Jiang, Y.; Zhao, H.; Liang, J.; Yue, L.; Li, T.; Luo, Y.; Liu, Q.; Lu, S.; Asiri, A. M.; Gong, Z.; Sun, X. Anodic oxidation for the degradation of organic pollutants: anode materials, operating conditions and mechanisms. A mini review. *Electrochem. Commun.* **2021**, *123*, No. 106912.

(37) Jung, H.; Pham, T.-T.; Shin, E. W. Interactions between ZnO nanoparticles and amorphous g-C₃N₄ nanosheets in thermal formation of g-C3N4/ZnO composite materials: The annealing temperature effect. *Appl. Surf. Sci.* **2018**, *458*, 369−381.

(38) Naik, G. K.; Majhi, S. M.; Jeong, K.-U.; Lee, I.-H.; Yu, Y. T. Nitrogen doping on the core-shell structured Au@TiO₂ nanoparticles and its enhanced photocatalytic hydrogen evolution under visible light irradiation. *J. Alloys Compd.* **2019**, *771*, 505−512.

(39) Chen, Y.; Xu, M.; Wen, J.; Wan, Y.; Zhao, Q.; Cao, X.; Ding, Y.; Wang, Z. L.; Li, H.; Bian, Z. Selective recovery of precious metals through photocatalysis. *Nat. Sustainability* **2021**, *4*, 618−626.

(40) Pan, H.; Steiniger, A.; Heagy, M. D.; Chowdhury, S. Efficient production of formic acid by simultaneous photoreduction of bicarbonate and oxidation of glycerol on gold-TiO$_2$ composite under solar light. *J. CO$_2$ Util.* **2017**, *22*, 117−123.

(41) Jedsukontorn, T.; Saito, N.; Hunsom, M. Photoinduced glycerol oxidation over plasmonic Au and AuM (M = Pt, Pd and Bi) nanoparticle-decorated TiO$_2$ photocatalysts. *Nanomaterials* **2018**, *8*, 269.

(42) Schünemann, S.; Dodekatos, G.; Tüysüz, H. Mesoporous silica supported Au and AuCu nanoparticles for surface plasmon driven glycerol oxidation. *Chem. Mater.* **2015**, *27*, 7743−7750.

(43) Khataee, A.; Aleboyeh, H.; Aleboyeh, A. Crystallite phase-controlled preparation, characterisation and photocatalytic properties of titanium dioxide nanoparticles. *J. Exp. Nanosci.* **2009**, *4*, 121−137.

(44) Shu, Y.; Chen, H.; Chen, N.; Duan, X.; Zhang, P.; Yang, S.; Bao, Z.; Wu, Z.; Dai, S. A principle for highly active metal oxide catalysts via NaCl-based solid solution. *Chem* **2020**, *6*, 1723−1741.

(45) Naldoni, A.; Riboni, F.; Marelli, M.; Bossola, F.; Ulisse, G.; Di Carlo, A.; Píš, I.; Nappini, S.; Malvestuto, M.; Dozzi, M. V.; et al. Influence of TiO$_2$ electronic structure and strong metal−support interaction on plasmonic Au photocatalytic oxidations. *Catal. Sci. Technol.* **2016**, *6*, 3220−3229.

(46) Yamada, K.; Miyajima, K.; Mafuné, F. Thermionic emission of electrons from gold nanoparticles by nanosecond pulse-laser excitation of interband. *J. Phys. Chem. C* **2007**, *111*, 11246−11251.

(47) Wang, C.; Astruc, D. Nanogold plasmonic photocatalysis for organic synthesis and clean energy conversion. *Chem. Soc. Rev.* **2014**, *43*, 7188−7216.

(48) Li, L.; Chen, H.; Li, L.; Li, B.; Wu, Q.; Cui, C.; Deng, B.; Luo, Y.; Liu, Q.; Li, T.; et al. La-doped TiO2 nanorods toward boosted electrocatalytic N$_2$-to-NH$_3$ conversion at ambient conditions. *Chin. J. Catal.* **2021**, *42*, 1755−1762.

(49) Xu, Z.; Liang, J.; Wang, Y.; Dong, K.; Shi, X.; Liu, Q.; Luo, Y.; Li, T.; Jia, Y.; Asiri, A. M.; et al. Enhanced Electrochemical H$_2$O$_2$ Production via Two-Electron Oxygen Reduction Enabled by Surface-Derived Amorphous Oxygen-Deficient TiO$_{2-x}$. *ACS Appl. Mater. Interfaces* **2021**, *13*, 33182−33187.

(50) Wu, T.; Zhao, H.; Zhu, X.; Xing, Z.; Liu, Q.; Liu, T.; Gao, S.; Lu, S.; Chen, G.; Asiri, A. M.; et al. Identifying the origin of Ti3+ activity toward enhanced electrocatalytic N2 reduction over TiO$_2$ nanoparticles modulated by mixed-valent copper. *Adv. Mater.* **2020**, *32*, No. 2000299.

(51) Chen, H.; Liang, J.; Li, L.; Zheng, B.; Feng, Z.; Xu, Z.; Luo, Y.; Liu, Q.; Shi, X.; Liu, Y.; et al. Ti$_2$O$_3$ nanoparticles with Ti^{3+} sites toward efficient NH$_3$ electrosynthesis under ambient conditions. *ACS Appl. Mater. Interfaces* **2021**, *13*, 41715−41722.

(52) Wu, T.; Zhu, X.; Xing, Z.; Mou, S.; Li, C.; Qiao, Y.; Liu, Q.; Luo, Y.; Shi, X.; et al. Greatly improving electrochemical N2 reduction over TiO$_2$ nanoparticles by iron doping. *Angew. Chem., Int. Ed.* **2019**, *58*, 18449−18453.

(53) Chen, Q.; Ma, C.; Yan, S.; Liang, J.; Dong, K.; Luo, Y.; Liu, Q.; Li, T.; Wang, Y.; Yue, L.; et al. Greatly facilitated two-electron electroreduction of oxygen into hydrogen peroxide over TiO$_2$ by Mn doping. *ACS Appl. Mater. Interfaces* **2021**, *13*, 46659−46664.

(54) Boyen, H.-G.; Kästle, G.; Weigl, F.; Koslowski, B.; Dietrich, C.; Ziemann, P.; Spatz, J. P.; Riethmüller, S.; Hartmann, C.; Möller, M.; et al. Oxidation-resistant gold-55 clusters. *Science* **2002**, *297*, 1533−1536.

(55) Etacheri, V.; Di Valentin, C.; Schneider, J.; Bahnemann, D.; Pillai, S. C. Visible-light activation of TiO$_2$ photocatalysts: Advances in theory and experiments. *J. Photochem. Photobiol., C* **2015**, *25*, 1−29.

(56) Yogi, C.; Kojima, K.; Takai, T.; Wada, N. Photocatalytic degradation of methylene blue by Au-deposited TiO$_2$ film under UV irradiation. *J. Mater. Sci.* **2009**, *44*, 821−827.

(57) Alshakhanbeh, M.; Ahmed, M.; Abou-Gamra, Z.; Madien, H. Influence of dispersion of various proportions of metallic gold nanoparticles on the optical and photocatalytic properties of titania. *Mater. Sci. Energy Technol.* **2020**, *3*, 429−439.

(58) Arias, M.-C.; Aguilar, C.; Piza, M.; Zarazua, E.; Anguebes, F.; Anguebes, F.; Anguebes, F.; Anguebes, F.; Cordova, V. Removal of the Methylene Blue Dye (MB) with Catalysts of Au-TiO$_2$: Kinetic and Degradation Pathway. *Mod. Res. Catal.* **2021**, *10*, 1.

(59) Mai, N. T. T.; Nga, N. K.; Hue, D. T. M.; Dung, T. N.; Chinh, H. D.; Huy, T. Q. Characterization of Co^{2+}-and Fe^{3+}-Codoped TiO$_2$ Nanomaterials for Photocatalytic Degradation of Organic Pollutants under Visible Light Irradiation. *Adsorpt. Sci. Technol.* **2021**, *2021*, No. 9193052.

(60) Medina, D.; Anderson, C. G. A review of the cyanidation treatment of copper-gold ores and concentrates. *Metals* **2020**, *10*, 897.

(61) Augugliaro, V.; Gálvez, J. B.; Vázquez, J. C.; López, E. G. a.; Loddo, V.; Muñoz, M. L.; Rodríguez, S. M.; Marcı, G.; Palmisano, L.; Schiavello, M.; et al. Photocatalytic oxidation of cyanide in aqueous TiO$_2$ suspensions irradiated by sunlight in mild and strong oxidant conditions. *Catal. Today* **1999**, *54*, 245−253.

(62) Murcia, J.; Navío, J.; Hidalgo, M. Insights towards the influence of Pt features on the photocatalytic activity improvement of TiO$_2$ by platinisation. *Appl. Catal., B* **2012**, *126*, 76−85.

(63) Chen, D.; Ray, A. K. Removal of toxic metal ions from wastewater by semiconductor photocatalysis. *Chem. Eng. Sci.* **2001**, *56*, 1561−1570.

(64) Yang, Z.; Lu, J.; Ye, W.; Yu, C.; Chang, Y. Preparation of Pt/TiO$_2$ hollow nanofibers with highly visible light photocatalytic activity. *Appl. Surf. Sci.* **2017**, *392*, 472−480.